

Enhancement of Photocatalytic Degradation of MB by Recyclable Li/Mn₃O₄ Thin films.

M. A. Amara

Universite de Tunis El Manar Faculte des Sciences de Tunis

T. Larbi

Universite de Tunis El Manar Faculte des Sciences de Tunis

N. Mahdhi

Universite de Tunis El Manar Faculte des Sciences de Tunis

Faycel saadallah (✉ faycel1@yahoo.fr)

Centre de Recherches et Technologies de l'Energie Laboratoire de Photovoltaïque

<https://orcid.org/0000-0002-7105-1599>

M. Amlouk

Université de Tunis El manar faculte des sciences de Tunis

Research Article

Keywords: Li/Mn₃O₄ physical mixture, Crystalline structure, Optical properties, Wettability, Impedance spectroscopy, Photocatalysis

Posted Date: February 25th, 2021

DOI: <https://doi.org/10.21203/rs.3.rs-239449/v1>

License:  This work is licensed under a Creative Commons Attribution 4.0 International License.

[Read Full License](#)

Version of Record: A version of this preprint was published at Journal of Materials Science: Materials in Electronics on March 29th, 2021. See the published version at <https://doi.org/10.1007/s10854-021-05756-2>.

Enhancement of photocatalytic degradation of MB by recyclable Li/Mn₃O₄ Thin films.

M. A. Amara^a, T. Larbi^a, N. Mahdhi^b, F. Saadallah^{c,*}, M. Amlouk^a

^a *Unité de physique des dispositifs à semi-conducteurs, Faculté des sciences de Tunis, Tunis El Manar University, 2092 Tunis, Tunisia.*

^b *Laboratoire Matériaux, Organisation et Propriétés, Campus Universitaire El Manar, Tunis 2092, Tunisia.*

^c *Laboratoire de Photovoltaïque LPV, CRTEn Borj Cedria, Tunisia.*

*Corresponding author: e-mail: *Faycell@yahoo.fr*

Abstract

Thin films of physical--mixture of Hausmannite Mn₃O₄ and lithium (Li) are synthesized by spray pyrolysis technique. Structural, morphological, optical, electrical, wettability and photocatalytic properties have been investigated. X-ray diffraction (XRD) and Raman spectra, Scanning electron microscope (SEM) images and electrical measurements show that Li nanoparticles are formed both on top surface of the film and inside grain boundaries. Bandgap and Urbach energies and optical relaxation time have been determined from transmittance T and reflectance R spectra. Impedance spectroscopy shows that charge separation increases with Li content, which improves photocatalytic efficiency of the film. The best photocatalytic efficiency is obtained for Li/Mn ratio of 15%. Indeed, the degradation of methylene blue (MB) under ultraviolet (UV) and visible light exposure, is improved by a factor of 5.7 and 2.4 respectively, when compared to undoped Mn₃O₄. In addition, this film exhibits a high photostability (10 cycles consecutively) under solar light. On the other hand, hydrophobicity reveals the hydrophilic character of the films.

Keywords : Li/Mn₃O₄ physical mixture; Crystalline structure; Optical properties; Wettability; Impedance spectroscopy; Photocatalysis.

Introduction

During the past decade, manganese oxide Mn_3O_4 has attracted researchers' curiosity due to its magnetic behavior, which is sensitive to crystal size at low temperature [1]. It is also used as anode materials for lithium-ion batteries [2–4], and supercapacitor applications [5,6]. Recently, Mn_3O_4 nanoparticles show moderate antibacterial activity against bacteria V [7]. On the other hand, Mn_3O_4 is a stable to corrosion, non-toxic and has good environmental compatibility, so it is a good candidate for sustainable energy devices.

Many techniques had been used for the synthesis of Mn_3O_4 thin films, including chemical bath deposition technique, pulsed laser ablation, and SILAR (Successive Ionic Layer Adsorption and Reaction) method [8–10]. In this work, we have prepared Mn_3O_4 thin films, by the spray pyrolysis technique, which is a simple, effective and cheap method with controllable reaction and large scale production of samples. Hausmannite Mn_3O_4 , is a multivalent oxide, that crystallizes in a spinel tetragonal structure with manganese ions (Mn^{3+}) in the octahedral sites and (Mn^{2+}) in the tetrahedral ones, respectively. This duality among sites is the origin of its important characteristics, which can be improved through metal ion doping. For instance, copper doped Mn_3O_4 microcrystal is an excellent reagent for the decomposition of organic contaminants in water [11]. Furthermore, Zhao et al. synthesized Sn-doped Mn_3O_4/C nanocomposites for supercapacitor electrode with higher capacitance [12]. Moreover, Li et al. [13] showed that Cr doping could enhance ferromagnetic properties of Mn_3O_4 nanowires. This material is a good candidate for photodegradation of organic dyes, since ferromagnetic materials such as Fe_3O_4 are confirmed as good photocatalysts. [14]

Likewise, previous work have demonstrated that the effect of Cr doping on physical properties of Mn_3O_4 thin films are very promising in the field of optoelectronics, photothermal conversion and chemical sensing [15]. In this context, Li is an efficient electron donor owing to its electronic states. It is also, an appropriate doping element to improve the physical properties of many transition metal oxides. For example, Li et al. [16] demonstrated that electrochemical performance and discharge capacity of NiO films are boosted by Li doping. Moreover, numerical simulation and experiments show that stochastic nonlinear dynamic characteristics and safe basin of Li-doped graphene are helpful for hydrogen storage field [17]. Moreover, previous works have demonstrated that addition of Li and Zr to Mn_3O_4 thin films leads to an enhanced response toward low ethanol concentration [18, 19]. Mn_3O_4 has a large potential in heterogeneous catalysis, in particular advanced oxidation techniques of H_2O_2 and degradation of dyes [20–22]. This photocatalytic activity can be improved by metal doping which increases free carrier lifetime. Recently, Kanwal et al. showed that

Mn₃O₄/Al₂O₃ heterostructure exhibits a bandgap narrowing and enhancement of charge separation due to a strong interfacial contact [23]. The same behavior was obtained by Jamila et al. for N and Bi doped carbon quantum dots on Mn₃O₄. They found that N and Bi doping induces a photoluminescence quenching leading to enhancement of photocatalytic activity [24].

In this paper, we have studied the effect of Li addition on the structural, electrical and optical properties of the Mn₃O₄ thin film. These properties are related with catalytic activity of the Mn₃O₄ thin film to enhance its photocatalytic performance in the visible region. The results of this study may be of interest for applications in photocatalysis and optoelectronic domains. Finally, recovering the photocatalyst after degradation of organic compounds remains a major obstacle to this technique. In order to avoid this problem, photocatalyst films are fixed on glass substrate.

2. Experimental procedure

2.1. Synthesis of physical mixture Li/Mn₃O₄

Physical mixture Li/Mn₃O₄ thin films are synthesized by spray pyrolysis technique. The sprayed solution is prepared by dissolving of 0.1 mole of manganese chloride MnCl₂(H₂O)₄ and LiCl in 100 ml deionized water. Four values of concentration ratio [Li]/[Mn] are used : 3, 6, 9 and 15 at% .The resulting solution is sprayed at a rate of 6 ml/min through a fine nozzle onto glass substrate preheated at 350 °C. The obtained thin films are annealed for 3 hours at 450 °C in air.

2.2. Characterization techniques

Firstly, structure and morphology of all samples are examined using XRD (X-Ray Diffraction) (“XPERT-PRO” diffractometer with Cu K α radiation at a wavelength $\lambda = 1.542 \text{ \AA}$), scanning electron microscope SEM (JEOL-JSM 5400), Raman spectroscopy (Jobin Yvon Horibra LABRAM-HR with the excitement source He-Ne 632 nm laser). Then, electrical conductivity was determined by an impedance meter (Hewlett-Packard 4192 analyzer) at a temperature of 250 °C in the frequency range 1 KHz–12.6 MHz. Thereafter, contact angle is measured by the Drop Shape Analyzer DSA100 system from KRÜSS. The deposit of the droplet of volume 5 μl and the recording of the contact angle are piloted automatically by a specific software. Appropriate model is used to calculate surface energy from the measurement of contact angle between distilled water and thin film [25]. Finally, optical transmittance T, reflectance R and absorbance A spectra of Mn₃O₄ films are

characterized by UV-visible spectroscopy (SHIMADZU UV 3100 spectrophotometer). The experiences of photocatalytic decomposition of methylene blue (MB) dye are performed by taking (6 or 20 mL) of 3 mg/L of MB solution to which are added the catalysts with $2 \times 2 \text{ cm}^2$ surface. The solution was stirred so as to improve exchanges between catalyst surface and MB solution. Different light beams are used to irradiate the solution at room temperature ($\approx 25^\circ\text{C}$). 35W Xenon lamp (H1 6000K Xenon Lamp HID) is considered as a visible light source (emission spectrum of 400 to 800 nm), 16W lamp (Philips TUV G8 T5 Germicidal, $\lambda = 253.7 \text{ nm}$) is used as ultra-violet (UV) light source and sunlight was the third alternative. According to the Beer–Lambert law, the absorbance A and concentration C of MB are proportional, so the degradation efficiency η of MB can be determined by applying the following equation: [26, 27]

$$\eta = \frac{A_0 - A}{A_0} \times 100\% = \frac{C_0 - C}{C_0} \times 100\% \quad (1)$$

Where C_0 , A_0 and C , A are the concentration and absorbance of MB when the reaction time is 0 and t, respectively. To compare the catalytic performances of the Li/Mn₃O₄ physical mixtures thin films at different Li contents, the degradation experiments of MB, model substrate used extensively for dyeing wool, silk, cotton and other industries, are realized in the same conditions for all the samples.

3. Results and discussion

3.1. Structural properties

XRD patterns of Li/Mn₃O₄ thin films with Li ratio ranging from 0 to 15%, are shown in **Fig. 1**. All diffraction peaks match very well with tetragonal hausmannite Mn₃O₄ structure according to JCPDS [01-075-1560] card [28]. This result is in good agreement with previous works [29]. Doping of Mn₃O₄ at low Li rate (3 and 6%) improves the sample crystallinity leading to an enhancement of XRD intensity. For the sample doped at 6% , the main peak at $2\theta = 18^\circ$ corresponding to (101) preferential orientation, exhibits the maximum intensity. At 9% of Li rate, XRD peaks are reduced due to partial destruction of crystalline structure and increased surface roughness. Indeed, this sample presents the maximum values of microstrain and dislocations density. At 15%, peak intensity increases owing to lower dislocations and microstrain as well as improved film crystallinity, since crystallite size has clearly increased (Table 1).

Positions and profiles of XRD peaks can be used to calculate lattice constants (a and c), grain size (D), microstrain (ε) and dislocation density (δ) which is related to optical and photocatalytic properties. These parameters are calculated using the following equations [30]:

$$\left\{ \begin{array}{l} D = \frac{0.9\lambda}{\beta \cos \theta} \quad (2) \\ \varepsilon = \frac{\beta}{4 \tan \theta} \quad (3) \\ \delta = \frac{1}{D^2} \quad (4) \end{array} \right.$$

Where θ (in radian) is the Bragg diffraction angle, β (in radian) is the full width at half-maximum (FWHM) of the most intense peak and λ is the X-ray wavelength. On the other hand, lattice constants (a and c) for tetragonal structure, are determined by :

$$\frac{1}{d_{hkl}^2} = \frac{h^2 + k^2}{a^2} + \frac{l^2}{c^2} \quad (5)$$

Where (h, k, l) are Miller indices and d_{hkl} is the inter-planar distance. In the same context, absolute variations of cell volume and crystallite size are given by:

$$\left\{ \begin{array}{l} \Delta v = \frac{v_0 - v}{v_0} \times 100\% \quad (6) \\ \Delta D = \frac{D_0 - D}{D_0} \times 100\% \quad (7) \end{array} \right.$$

Where v_0 , D_0 and v , D are cell volume and crystallite size of pure Mn_3O_4 and Li/Mn_3O_4 thin films. All calculated parameters are given in Table 1. We notice that cell parameters ($a = 5.738 \text{ \AA}$, $c = 9.468 \text{ \AA}$ and $v = 311.706 \text{ \AA}^3$) are independent from Li content. No peaks related to Li oxides or other species are observed in all XRD spectra. Moreover, substitution of Mn element by Li is limited due to possibility of a single bond for Li while manganese may establish 2 or 3 bonds. Based on these results, we conclude that cell parameters and chemical composition of Mn_3O_4 are not affected by Li. This confirms the assumption that Li atoms are not incorporated into Mn_3O_4 matrix, but remain at the surface of Mn_3O_4 nanoparticles. These results are in good agreement with those obtained by Ben Said et al [22], which proved that Zr is partially incorporated into the Mn_3O_4 nuclei, it grows as nanoparticles at the film surface and in the grain boundaries. Similar results have been also reported in the literature, concerning the oxidation of zinc in presence of noble metals (Ag, Pt) which leads to pure metal nanoparticles at the surface of ZnO film[31-33]. On the other hand, main XRD peaks

are used to determine crystallite size, microstrain (ϵ) and dislocation density (δ). These parameters are obviously, affected by added Lithium.

Table 1: Structural parameters of Li/Mn₃O₄ physical mixtures thin films at different Li content.

Sample	Cell parameters				Crystallite size D (nm) + ΔD (%)	Dislocation density δ (10 ¹³ lines/m ²)	Microstrain (ϵ) (10 ⁻³)
	a (Å)	c (Å)	c/a	Cell volume v (Å ³) + Δv (%)			
Mn ₃ O ₄ Pure	5.738	9.468	1.650	311.706 + 0	137.404 + 0	5.297	1.605
Li/Mn ₃ O ₄ : 3%	5.725	9.464	1.653	310.217 + 0.47	120.260 + 12.5	6.914	1.831
Li/Mn ₃ O ₄ : 6%	5.739	9.459	1.648	311.547 + 0.05	96.178 + 30.0	10.810	2.290
Li/Mn ₃ O ₄ : 9%	5.729	9.453	1.650	310.266 + 0.46	96.178 + 30.0	10.810	2.290
Li/Mn ₃ O ₄ :15%	5.738	9.465	1.649	311.654 + 0.02	192.466 – 40.1	2.699	1.146

Raman spectra of Li/Mn₃O₄ thin films shown in Fig. 2, are composed of two small peaks at 315, 370 and a sharp peak at 655 cm⁻¹. The main peak at 655 cm⁻¹ is owed to Mn-O vibration mode (A_{1g}) [24]. Raman peak positions and bandwidths are similar to those of pure Mn₃O₄ [34]. We conclude that Mn₃O₄ crystalline structure is not affect by Lithium.

Raman peaks intensity decreases when Li doping rate increases from 0 to 6%, then it increases from 6 to 15%. The main reason of this behavior is the variation in absorbance of the incident laser beam due to bandgap shifts. These variations will be discussed in the following section 3.2.

The variation of intensity can also be related to the variation of crystallite size and dislocation density. From 0 to 6% of Li, the crystallite size is reduced and dislocations are enhanced which causes a loss of light by diffusion and reduces Raman scattering effect. This behavior is reversed when Li rate increases from 6% to 15%.

SEM images (Fig. 3(a-e)) confirms the results obtained by XRD and Raman spectra. We observe few grains distributed on the film surface, resulting from agglomeration of small Li nanoparticles. Similar results have been reported by Shinde et al. [35] which observed a few aggregated Li particles distributed on the surface of Li doped ZnO films. SEM images reveal a decrease of Mn₃O₄ nanoparticle size when Li doping rate is increased from 0 to 9%. In particular at 6% we notice the formation of nanorods of Mn₃O₄ which can explain the increase

of XRD peak corresponding to (101) orientation. At doping rate of 15%, the nano-grain size is obviously enhanced in agreement with XRD calculations.

Table 2 shows the RMS roughness of Li/Mn₃O₄ physical mixtures. The surface roughness increases by increasing Li rate up to 9%, then it decreases slightly at 15% which corresponds to largest crystallite size and best crystallinity. These factors are of most importance in photocatalytic activity.

3.2. Optical study

Transmittance $T(\lambda)$ and reflection $R(\lambda)$ spectra of Li/Mn₃O₄ thin films are shown in **Fig. 4 (a)** and Absorbance in Fig.4(b) . We find that optical transmittance increases with Li content in the visible and near infrared region. Therefore, penetration depth of light into the films is increased leading to excitation of electrons and holes inside the film volume. Similar result has been reported in literature for Li doped ZnO thin films [35]. In addition, Li doping induces absorption edge shift toward low wavelengths. Optical absorption spectra (Fig.4 (c)) obtained from absorbance spectra (Fig. 4(b)), are used to determine the band gap energy E_g following the Tauc law [17]:
$$\alpha \cdot h\nu = A(h\nu - E_g)^{1/2} \quad (8)$$

We have also determined Urbach energy E_u from the equation [36]:

$$\alpha = \alpha_0 \exp(h\nu/E_u) \quad (9)$$

Where α is the absorption coefficient and $E = h\nu$ the photon energy of incident light.

The obtained energy values of E_g and E_u are given in Table 2. We notice that band gap energy increases from 2.23 to 2.82 eV as Li ratio increases from 3% to 6%, then decreases slightly to 2.67 eV for the film at 15%. These bandgap shifts may explain the variations of Raman peaks intensity. Indeed, the blue shift obtained from 3 to 6% of Li lead to a drop of the optical absorbance (Fig.4 (b)), especially for the wavelength of the Raman laser (632 nm), which leads to a reduction of the Raman effect. From 6% to 15% of Li, the Raman peaks are enhanced as the optical absorption at the laser wavelength is improved.

The band gap energy depends on several factors such as effective mass of charge carriers and Bohr radius. For a semiconductor crystal, the exciton is usually delocalized over a distance much longer than the lattice constant called Bohr radius. When the dimension of the crystallite becomes near to Bohr radius, the exciton is confined and consequently its electronic properties start to change [37, 38].

Same results have been reported in previous works on ZnO and WO₃ doped with Lithium [39, 40] where localized states appear in the band gap due to Li induced-defects. The analysis of

Urbach energy shows that the width of localized states increases with Li content. Indeed, dislocation density, microstrain (Table 1) and roughness (Table 2) are markedly enhanced by Li doping from 3% to 9%. At 15% of Li, the film exhibits a high value of Urbach energy despite the decrease of dislocations density. This is probably due to other defects induced by Li cations, such as oxygen vacancies and interstitial Mn. The broadening of band gap tails is of a great benefit for photocatalytic activity since the charge hopping between these localized states is improved [41].

On the other hand, dielectric calculations are used to determine optical relaxation time τ_{op} which correspond to the lifetime of photo-excited carriers. In the near infrared region, optical relaxation time τ_{op} is related to real and imaginary parts (ϵ_1 and ϵ_2) of the complex dielectric constant ϵ via the relation [42, 43].

$$\frac{\epsilon_2}{|\epsilon_1 - \epsilon_\infty|} = \frac{\lambda}{2\pi c \tau_{op}} \quad (10)$$

Where ϵ_∞ is the dielectric constant at high frequencies, λ is the wavelength and c is the light celerity.

The calculated values of relaxation time are shown in Table 2. We notice that pure Mn_3O_4 film has the smallest value of relaxation time that increases with Li doping. The maximum value is obtained for 15% of Li rate, since the film exhibits highest crystallite size, best crystallinity and minimum rate of defects.

Table 2: Optical parameters and RMS roughness of Li/ Mn_3O_4 physical mixtures thin films at various Li content.

Sample	E_g (eV)	E_U (meV)	τ_{op} (10^{-13} s)	R_q (nm)
Mn₃O₄ Pure	2.23	354	1.45	17.82
Li/Mn₃O₄: 3%	2.7	614	2.47	25.21
Li/Mn₃O₄: 6%	2.82	637	3.14	33.55
Li/Mn₃O₄: 9%	2.75	750	1.75	57.43
Li/Mn₃O₄:15%	2.67	765	4.46	53.85

3.3. Photoluminescence

Photoluminescence spectroscopy (PL) is used to study the radiative recombination mechanisms of Li doped Mn_3O_4 films when irradiated by 488 nm laser beam. For all samples, PL spectra (**Fig. 5**) show a broad and intense peak centered at 694 nm neighbored by a small peak at 640 nm. The broadness of

main peak is due to many defects caused by dislocation and fractal morphology of the nanostructured surface resulting from deposition technique and Li doping effects. This phenomenon is enhanced by structural defects such as interstitial Mn and oxygen vacancies. The curves show red luminescence at 640 and 693 nm corresponding to energies (1.77 and 1.92 eV) lower than the band gap energy of Mn₃O₄ films. These peaks are originated from the optical transitions due to structural disorder-induced localized states in the bandgap [44].

We conclude that radiative transitions occur between deep levels induced by defects and the valence (or conduction) band [45].

However, increasing Li rate reduces noticeably the PL main peak. Indeed, the growth of Mn₃O₄ small grains around Li nanoparticles at the film surface and the raise of Li-induced defects provokes the inhibition of radiative recombinations of electron-hole pairs through the hopping process. For high Li doping rate (15%), the main peak drops drastically as radiative recombinations are reduced leading to the improvement of photogenerated free-carrier lifetime.

3.3. Impedance spectroscopy

Impedance spectroscopy is a reliable technique to study the electrical properties of a material and to disclose the efficiency of charges carrier trapping. Thus, this technique is carried out to evaluate the chemical interaction between Mn₃O₄ thin film and Li nanoparticles by electrical conduction. Fig. 6 shows the complex impedance spectra obtained by plotting the imaginary part (-Z'') of the impedance versus corresponding real part (Z'). The intercepts of semi-circular impedance curves with real axis (Z') correspond to the resistance values. The decrease of the curvature radius while increasing Li content, implies a decrease of electrical resistance R. Indeed, adding metallic atoms such as Li leads to great amount of free carriers injected in the semiconductor material which enhances its electrical conductivity. This result is in agreement with previous works [35, 46] which proved that Li doping improves electrical conductivity and electron mobility for ZnO thin films. Similar results on Mn₃O₄-MnO₂ composite had been reported by Zhao et al. [7] who found that the sample giving smallest radius of impedance curve yields the highest photocurrent. The analysis of experimental data of all the materials shows that the semi-circles are slightly sunken. This effect is well described by the Cole–Cole model in which a polarization phenomenon with a distribution of relaxation time occurs in the material. According to this model, the complex impedance is given by the equation [36]:

$$Z'' = \frac{R}{1 + (i\omega\tau_{el})^\alpha} \quad (11)$$

Where $\tau_{el} = RC$ is the mean value of relaxation time distribution, ω is the angular frequency and α is a parameter which characterizes the relaxation time distribution. In order to study relaxation time, electrical conductivity and capacity of Li/Mn₃O₄ thin films, we have plotted (-Z'') versus frequency in Fig.7. The elements values of the equivalent electric circuit are ported on Table 3.

Table 3: Values of Cole–Cole fitting model parameters.

Sample	R (MΩ)	C (10 ⁻¹¹ F)	τ_{el} (10 ⁻⁵ s)	α (for Z _{Cole–Cole})
Li/Mn ₃ O ₄ : 3%	2.867	0.707	2.026	0.965
Li/Mn ₃ O ₄ : 6%	23.776	0.139	3.307	0.901
Li/Mn ₃ O ₄ : 9%	11.325	0.503	5.699	0.967
Li/Mn ₃ O ₄ :15%	5.380	0.832	4.476	0.950

The maximum of imaginary part (-Z'') shifts toward low frequencies as the Li content increases suggesting an increase of relaxation time average-value and a longer mean free path of charge carriers. Meanwhile, film capacitance C is found to increase with Li content which reveals an enhancement of charge separation in Li/Mn₃O₄ films. Indeed, a schottky junction appears between Li grains and the p-type Mn₃O₄ film [47]. Charge separation provokes the enhancement of carrier lifetime [48] which is the determining factor in photocatalysis process [26, 49–53].

3.4. Wettability study

Table 4 presents the measured contact angles of water and MB solution at the surface of Li/Mn₃O₄ film. It is clear that contact angle is reduced by Li doping. The contact angle decreases as the Li content increases until reaching the minimum value of 30.3° for 15% of Li ratio. Such behavior is owed to the increase of film roughness. Besides hydrophilic character of Li/Mn₃O₄ film, the reduction of contact angle enhances the adsorption of MB molecules at the film surface, which improves the photo-degradation of the organic pollutant. This result agrees very well with several previous studies [54–56] which showed that high surface roughness can improve the hydrophilicity as well as the surface energy leading to a better catalytic performance. The formation of Li nanoparticles increases the specific surface area, which enhances the adsorption of pollutant at the film surface [57, 58]. Surface energy

calculated from measured values of contact angle is found to be practically constant for different Li content. However, it is substantially higher for Li doped films compared to that of pure Mn_3O_4 thin film.

Table 4: Contact angle between water, the MB solution and the Li/ Mn_3O_4 thin films and the surface energy corresponding to the water contact angle as a function of Li content.

Li content (at. %)	Contact angle water(θ)	Surface energy (mN/m)	Contact angle solution MB (θ)
0	57.3	48.7	62.9
3	36.1	60.6	38.5
6	38	59.4	34.6
9	35.4	61	31.1
15	36.8	60.2	30.3

3.5. Photocatalytic activity

3.5.1 UV irradiation effect

Fig. 8 shows the absorption spectra of MB solution in presence of Li/ Mn_3O_4 thin film for 2 h under UV-light, at room temperature. Under the same conditions, a blank test is realized without film, in order to evaluate the self-degradation of MB, which is evaluated to about 9%. However, catalytic decomposition of MB in presence of Li/ Mn_3O_4 thin films increases with Li content. In the case of 15% ratio, we notice a degradation efficiency of about 5.7 times higher than that of pure Mn_3O_4 . Fig. 9 shows a satisfactory correlation between photocatalytic efficiency, electrical resistance and electric capacitance. It is found that photocatalytic activity is improved while increasing the film capacitance. However, it is reduced by the rise of electrical resistance. These results are in good agreement with previous work [35] on Li doped ZnO thin films. After 2h of exposure time, we obtain the elimination of 46% of MB molecules which is of the same order with the results obtained with Ag/ZnO nanoparticles (50%) [31]. On the other hand, catalytic activity is dependent on the size and distribution of Li nanoparticles. It can be suggested that particle with small size allows a better dispersion and thus a large number of active sites, thus improving the catalytic activity. This result is consistent with previous works [31, 52, 57, 59].

3.5.2 Visible light effect

Fig. 10 shows the absorption spectra of MB alone and in presence of Li/Mn₃O₄ thin films under visible light. At first, we notice a same rate for the degradation of MB in presence of pure Mn₃O₄ or without catalyst. Then, degradation activity is improved by Li doping and the efficiency is extended from UV to visible region. Indeed, under visible light the pure Mn₃O₄ catalyst exhibits no effect on MB degradation, however, a noticeable effect is seen with the sample doped at 15% of Li. Indeed, the efficiency of the physical mixture at 15% of Li is nearly 2.4 times better than that of pure Mn₃O₄, after 2 hours. We conclude that the sample at 15% Li possesses the best photocatalytic activity under UV and visible lights. This result is consistent with previous works [27, 31, 32, 35] on photocatalytic behavior of metal doped ZnO films.

The variation of photocatalytic efficiency and optical relaxation time with Li content is shown in Fig.11. The photocatalytic efficiency varies proportionally with the variation of optical relaxation time. This may be explained by the increase of photogenerated charges lifetime, which allows electrons and holes to react with water and oxygen before recombination. This result is confirmed by the degradation of visible photoluminescence seen above, especially for the sample with 15% of Li rate, which proves that carrier lifetime is enhanced while radiative recombinations are reduced by hopping effect.

Moreover, photocatalytic reaction is boosted by the great number of free electrons released by metallic Li atoms adjacent to Mn₃O₄ nanoparticles.

The degradation results analysis of MB under UV and visible light, and those of impedance spectroscopy experiments and optical absorption, reveal reliable information on the degradation mechanism of MB. The almost zero role of pure Mn₃O₄ to the degradation of MB allows deducing that the recombination of photogenerated electron-hole pairs in pure Mn₃O₄ is very fast which inhibits the degradation of MB pollutant. The Li addition to the Mn₃O₄ helps to reduce the electrical resistance and increases the capacity and the duration of optical relaxation. After light absorption, the photogenerated electrons can transfer from Mn₃O₄ to Li induced traps such as dislocations and oxygen vacancies. Thus, improving charge separation and carrier lifetime, which instigate the formation of hydroxyl radicals essential for MB degradation. Photocatalytic process suggested above is in agreement with previous works [31, 32, 60] which showed that noble metal particles helps the transmission of photoelectrons at the film surface and can be the instigator of photogeneration process.

3.5.3 Solar Energy-recyclability

Fig. 12 displays the evolution of MB degradation in the presence of Li/Mn₃O₄ at 15% as a function of exposure time to sunlight irradiation. For these experiments, 20 mL of MB solution is used, which correspond to 3.33 times as the volume exposed to UV and visible light source. The drop of absorption peak to baseline level showed that degradation of sub-products and the scission of bonds are perpetuated up to mineralization.

After 4h of exposure time, we obtain the elimination of 91 % of MB molecules which is of the same order with the results obtained with nitrogen doped carbon quantum dots (NCQD) on Mn₃O₄ (73-100 %) [24].

After irradiation for 6 h, we notice that about 2% of MB remains in aqueous solution, so the photodegradation of MB is practically complete.

Photocatalytic degradation of MB follows the pseudo-first order kinetics :

$$\ln(C/C_0) = -k t \quad (12)$$

Where C₀ and C are the MB concentration at t = 0 and t, respectively.

The degradation rate k for each sample is obtained from a linear fit of the curve ln(C₀/C) versus time given in Fig.13. This curve shows that photodegradation of MB molecules follows first-order reaction. The first-order degradation rate constants for Li doped Mn₃O₄ samples are found to increase with Li rate and the optimum value k = 7.6 10⁻³ min⁻¹ is obtained for 15% Li. This value is far from the rate obtained without catalyst which is below 0.9 10⁻³ min⁻¹.

The stability of Li/Mn₃O₄ at 15% of Li is investigated by comparing the MB absorbance with the same catalyst for the first degradation cycle and after 10 repetitive cycles. As shown in Fig.14, the Li/Mn₃O₄ (15%) catalyst conserve the same efficiency in the degradation of MB solution during the 10 cycles. This reveals that Li/Mn₃O₄ 15% catalyst has a high stability to be reused in degradation of MB. The high photostability of this catalyst is attributed to good crystalline structure of Li/Mn₃O₄ 15% which is due to annealing at 450°C for 3 h and doping by Li element that significantly reduced the density of defects and inhibits effectively the photo-corrosion of Mn₃O₄ thin film [61, 62]. On the other hand, photocatalytic efficiency can be attributed to the small size of Li nanoparticles, which improves oxygen adsorption at the catalyst surface [31, 63]. Finally, considering its recyclability and high photostability, we conclude that Li/Mn₃O₄ (15%) is a powerful photocatalyst under solar irradiation.

4 Conclusion

Li doped Mn_3O_4 have been successively deposited onto glass substrate by versatile spray pyrolysis technique. The influence of Li addition on structural, morphological, optical, electrical, and photocatalytic properties is investigated. XRD, Raman and electrical analyses reveal the existence of Li nanoparticles at the surface and in the grain boundaries of Mn_3O_4 thin films. Their size and distribution are determined by SEM images. Capacitance, electrical conductivity and optical lifetime are enhanced by Li doping. The increase of photo-carrier lifetime is confirmed by the drop of radiative recombination as photoluminescence peak is drastically reduced while increasing Li doping rate.

Wettability proved that liquid adsorption at the film surface is improved by Li nanoparticles. Moreover, photocatalytic activity of catalyst Mn_3O_4 is enhanced by increasing Li content in the film. Photocatalytic efficiency of thin films is attributed to long lifetime of photogenerated electron-hole pairs. For this purpose, the film should have low defect density, high crystallinity and spatial separation of charge carriers. The physical mixture Li/ Mn_3O_4 at 15% of Li rate, exhibited the highest photocatalytic efficiency for MB decomposition, 5.7 and 2.4 times higher than that obtained with pure Mn_3O_4 catalyst under UV and visible lights, respectively. It has been deduced that Li doping broaden the activity spectrum of Mn_3O_4 catalyst from UV to visible region, which allows a better exploitation of the free solar energy. Li/ Mn_3O_4 with optimal rate of 15% exhibits the highest photostability. Indeed, this film exhibits the same photocatalytic efficiency after 10 consecutive photocatalytic cycles. We conclude that it can be used as immobilized photocatalyst for water purification from organic pollutants and self-cleaning applications under sunlight.

References

- [1] L.X. Yang, Y.J. Zhu, H. Tong, W.W. Wang, G.F. Cheng, *J. Sol. State Chem.* 179, 1225 (2006).
- [2] D. Zhao, Q. Hao, C. Xu, *Electrochim. Acta* 180, 493 (2015).
- [3] M. Jing, H. Hou, Y. Yang, Y. Zhang, X. Yang, Q. Chen, X. Ji, *Electrochim. Acta* 155, 157 (2015).
- [4] M. Zhen, Z. Zhang, Q. Ren, L. Liu, *Mater. Lett.* 177, 21 (2016).

- [5] P.T.M. Bui, J.H. Song, Z.Y. Li, M.S. Akhtar, O.B. Yang, J. Alloys Compd. 694, 560 (2017).
- [6] A.A. Yadav, S.N. Jadhav, D.M. Chougule, P.D. Patil, U.J. Chavan, Y.D. Kolekar, Electrochim. Acta 206, 134 (2016).
- [7] A.N. Chowdhury, M.S. Azam, M. Aktaruzzaman, A. Rahim, J. Hazard. Mater. 172, 1229 (2009).
- [8] D.P. Dubal, D.S. Dhawale, R.R. Salunkhe, V.J. Fulari, C.D. Lokhande, J. Alloys Comp. 497, 166 (2010).
- [9] D. Yang, J. Power Sources 169, 8843 (2011).
- [10] D.P. Dubal, D.S. Dhawale, R.R. Salunkhe, S.M. Pawar, C.D. Lokhande, Appl. Surf. Sci. 256, 4411 (2010).
- [11] F. Wang, H.Q. Wu, Z.T. Lin, S.Y. Han, D. Wang, Y. Xue, Y.L. Sun, J. Sun, B. Li, Mater. Res. Bull. 45, 1567 (2010).
- [12] Y. Zhao, W. Ran, D.-B. Xiong, L. Zhang, J. Xu, F. Gao, Mater. Lett. 118, 80 (2014).
- [13] G.M. Li, X.B. Tang, S.Y. Lou, S.M. Zhoua, Appl. Phys. Lett. 104, 17310 (2014).
- [14] S. Shamaila, T. Bano and A. K. L. Sajjadi., Ceram. Inter. 43(17), 14672 (2017).
- [15] T. Larbi, A. Amara, L.B. Said, B. Ouni, M.H. Lakhdar, M. Amlouk, Mater. Res. Bull. 70, 254 (2015).
- [16] Y. Li, X. Li n, Z. Wang, H. Guo, T. Li, Ceram. Inter. 42, 14565 (2016).
- [17] J. Xu, J. Li, H. Wang, Z. Zhu, Inter. J. Hydrog. Ener. 41, 15740 (2016).
- [18] M.A. Amara, T. Larbi, A. Labidi, M. Karyaoui, B. Ouni, M. Amlouk, Mater. Res. Bulletin 75, 217 (2016).
- [19] L. Ben Said, A. Inoubli, B. Bouricha, M. Amlouk, Spectrochimica Acta Part A: Molecul. Biomol. Spect. 171, 487 (2017).
- [20] M. Y. Rizal, R. Saleh, A. Taufik, S. Yin, Environ. Nanotech. Monit. Manag. 15, 100408 (2021).
- [21] T. Shen, X. Shi, J. Guo, S. Yuan, Chem. Eng. J. 408, 128014 (2021).
- [22] J. Zhao, J. Nan, Z. Zhao, N. Li, J. Liu, F. Cui, Appl. Catal. B: Environ. 202, 509 (2017).
- [23] A. Kanwal, S. Sajjad, S. A. K. Leghari, M. N. Khan, Chinese. J. Chem. Engin. <https://doi.org/10.1016/j.cjche.2020.09.010>, *in Press*.
- [24] G.S. Jamila, S. Sajjad, S.A.K. Leghari, Y. Li, New J. Chem. 44, 11631 (2020)..
- [25] D. Li, A.W. Neumann, Adv. Coll. Interface Sci. 39, 299 (1992).

- [26] H. Ennaceri, D. Erfurt, L. Wang, T. Köhler, A. Taleb, A. Khaldoun, A. El Kenz, A. Benyoussef, A. Ennaoui, *Surf. Coat. Technol.* 298, 103 (2016).
- [27] N. Soltani, E. Saion, W.M. Mat Yunus, M. Navasery, G. Bahmanrokh, M. Erfani, M. Reza Zare, E. Gharibshahi, *Sol. Ener.* 97, 147 (2013).
- [28] A.D. Mighell, C.R. Hubbard, J.K. Stalick, M.A. Holomany, NBS*AIDS83, JCPDS-International Centre for Diffraction Data, Swarthmore, PA, U.S.A, 1983.
- [29] T. Larbi, B. Ouni, A. Boukhachem, K. Boubaker, M. Amlouk, *Mater. Res. Bulletin* 60, 457 (2014).
- [30] T. Larbi, M.A. Amara, B. Ouni, M. Amlouk, *Mater. Res. Bulletin* 95, 152 (2017).
- [31] L. Muñoz-Fernandez, A. Sierra-Fernandez, O. Milošević, M.E. Rabanal, *Advanc. Powd. Technol.* 27, 983 (2016).
- [32] Q. Deng, X. Duan, D.H.L. Ng, H. Tang, Y. Yang, M. Kong, Z. Wu, W. Cai, G. Wang, *Appl. Mater. Interf.* 4, 6030 (2012).
- [33] J. Cho, N. Salleh, C. Blanco, S. Yang, C.J. Lee, Y.W. Kim, J. Kim, J. Liu, *Nanoscale* 6, 3861 (2014).
- [34] G.C. Silva, F.S. Almeida, M.S.S. Dantas, A.M. Ferreira, V.S.T. Ciminelli, *Spectrochim. Acta Part A: Molecul. Biomolecul.Spect.* 100, 161 (2013).
- [35] S.S. Shinde, C.H. Bhosale, K.Y. Rajpure, *J. Photochem. Photobiol. B: Biology* 120, 1 (2013).
- [36] T. Larbi, A. Amara, B. Ouni, A. Inoubli, M. Karyaoui, A. Yumak, F. Saadallah, K. Boubaker, M. Amlouk, *J. Magnet.Magnet.Mater.* 387, 139 (2015).
- [37] M.R. Belkhedkar, A.U. Ubale, *J. Molecul. Struct.* 1068, 94 (2014).
- [38] H.J. Snaith, L.S. Mende, *Advanc. Mater.* 19, 3187 (2007).
- [39] P. Chanda, A. Gaura, A. Kumara, U-K. Gaur, *Ceram. Inter.* 40, 11915 (2014).
- [40] M. Kovendhan, D.P. Joseph, E.S. Kumar, A. Sendilkumar, P. Manimuthu, S. Sambasivam, C. Venkateswaran, R. Mohan, *Appl. Surf. Sci.* 257, 8127 (2011).
- [41] B. Ouni, M. Haj Lakhdar, R. Boughalmi, T. Larbi, A. Boukhachem, A. Madani, K. Boubaker, M. Amlouk, *J. Non-Crystal Sol.* 367, 1 (2013).
- [42] C. Mrabet, O. Kamoun, A. Boukhachem, M. Amlouk, T. Manoubi, *J. Alloys Comp.* 648, 826 (2015).
- [43] C. Mrabet, A. Boukhachem, M. Amlouk, T. Manoubi, *J. Alloys Comp.* 666, 392 (2016).
- [44] M.A. Mousa, M.M. Rashad, M.M. Mokhtar, Mahmoud E. El Shazli, *J. Bas. Environ. Sci.* 7, 171 (2020).

- [45] U. Ilyas, R.S. Rawat, T.L. Tan, P. Lee, R.Chen, H. D. Sun, F. Li and S. Zhang, *J. Appl. Phys.* 110, 093522 (2011).
- [46] H.J. Jeon, S.G. Lee, H. Kim, J.S. Park, *Appl. Surf. Sci.* 301, 358 (2014).
- [47] T. Larbi, M. Haj Lakhdar, A. Amara, B. Ouni, A. Boukhachem, A. Mater, M. Amlouk, *J. Alloys Comp.* 626, 93 (2015).
- [48] W. Kang, X. Jimeng, W. Xitao, *Appl. Surf. Sci.* 360, 270 (2016).
- [49] W. Choi, A. Termin, M.R. Hoffmann, *J. Phys. Chem. B* 98, 13669 (1994).
- [50] J.M. Herrmann, *Top. Catal.* 34, 49 (2005).
- [51] Y. Tian, T. Tatsuma, *J. Amer. Chem. Soc.* 127, 7632 (2005).
- [52] S. Kuriakose, V. Choudhary, B. Satpati, S. Mohapatra, *Beilstein J. Nanotechnol.* 5, 639 (2014).
- [53] L. Wang, X. Hou, F. Li, G. He, L. Li, *Mater. Lett.* 161, 368 (2015).
- [54] H. Ennaceri, A. Khaldoun, A. Benyoussef, T. Köhler, R. Sáez-Araoz, A. Ennaoui, *Advanc. Mater. Res.* 1119, 355 (2015). doi.org/10.4028/www.scientific.net/AMR.1119.355
- [55] S. Kuriakose, V. Choudhary, B. Satpati, S. Mohapatra, *Beilstein J Nanotechnol* 5, 639 (2014).
- [56] J. Zhang, K. Sasaki, E. Sutter, R.R. Adzic, *Science* 315, 220 (2007).
- [57] L. Xu, Y.L. Hu, C. Pelligra, C.H. Chen, L. Jin, H. Huang, S. Sithambaram, M. Aindow, R. Joesten, S.L. Suib, *Chem. Mater.* 21, 2875 (2009).
- [58] G.R. Li, T. Hu, G.L. Pan, T.Y. Yan, X.P. Gao, H.Y. Zhu, *J. Phys. Chem. C* 112, 11859 (2008).
- [59] D. Li, H. Haneda, *Chemosphere* 51, 129 (2003).
- [60] Q. Wang, B. Geng, S. Wang, *Environ. Sci. Technol.* 43, 8968 (2009).
- [61] H. Fu, T. Xu, S. Zhu, Y. Zhu, *Environ. Sci. Technol.* 42, 8064 (2008).
- [62] N. Kislov, J. Lahiri, H. Verma, D.Y. Goswami, E. Stefanakos, M. Batzill, *Langmuir* 25, 3310 (2009).
- [63] W.L. Ong, K.W. Yew, C.F. Tan, T.K. Tan Adrian, M. Hong, G.W. Ho, *RSC Adv.* 4, 27481 (2014).

Figure captions

Fig.1 XRD pattern of pure and Li doped Mn_3O_4 thin films.

Fig.2 Raman spectra of Li/ Mn_3O_4 physical mixtures thin films.

Fig.3 SEM images of Li/ Mn_3O_4 thin films at different Li contents:

0% (a), 3% (b), 6% (c), 9% (d), 15% (e)

Fig.4(a) Transmittance and reflectivity spectra of Li/ Mn_3O_4 thin films.

Fig.4(b) Absorbance of Li/ Mn_3O_4 thin films for different Li contents.

Fig.4(c) Absorption spectra of Li/ Mn_3O_4 thin films for different Li contents.

Fig.5 Photoluminescence spectra of Li/ Mn_3O_4 thin films.

Fig.6 Complex impedance spectra of Li/ Mn_3O_4 thin films.

Fig.7 Impedance imaginary-part Z'' versus frequency, for Li/ Mn_3O_4 thin films.

Fig.8 MB absorption spectra after degradation by Li/ Mn_3O_4 thin films under UV irradiation for 2h.

Fig.9 Degradation efficiency, electrical resistance and capacity of Li/ Mn_3O_4 thin layers.

Fig.10 MB absorption spectra in presence of Li/ Mn_3O_4 thin films after 2 h exposure to visible light.

Fig.11 Variations of photocatalytic efficiency and optical relaxation time versus Li content.

Fig.12 Absorption spectra of MB in presence of Li/ Mn_3O_4 at 15% of Li as a function of sunlight exposure time.

Fig.13 Photocatalytic degradation of MB by Li/ Mn_3O_4 at 15% of Li, under sunlight irradiation.

Fig. 14 Stability of physical mixture Li/ Mn_3O_4 at 15% of Li for photodegradation of MB under sunlight.

Declarations

Funding: Not applicable

Conflicts of interest/Competing interests: Not applicable

Availability of data and material: Not applicable

Code availability: Not applicable

Authors' contributions: Not applicable

Compliance with Ethical Standards

Disclosure of potential conflicts of interest: *Not applicable.*

Research involving Human Participants and/or Animals:

No Human or animal participants are involved.

Informed consent : *Not applicable.*

Figures

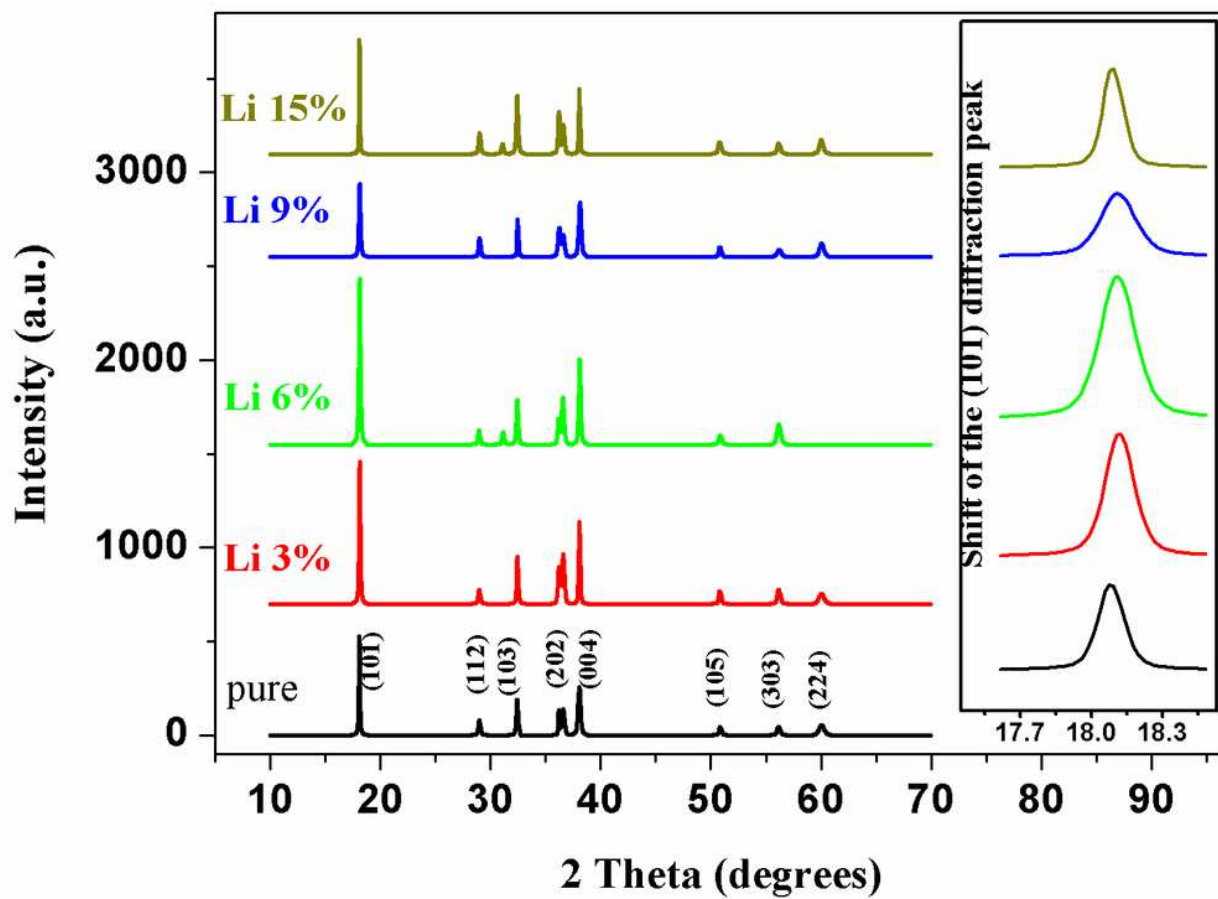


Figure 1

XRD pattern of pure and Li doped Mn₃O₄ thin films.

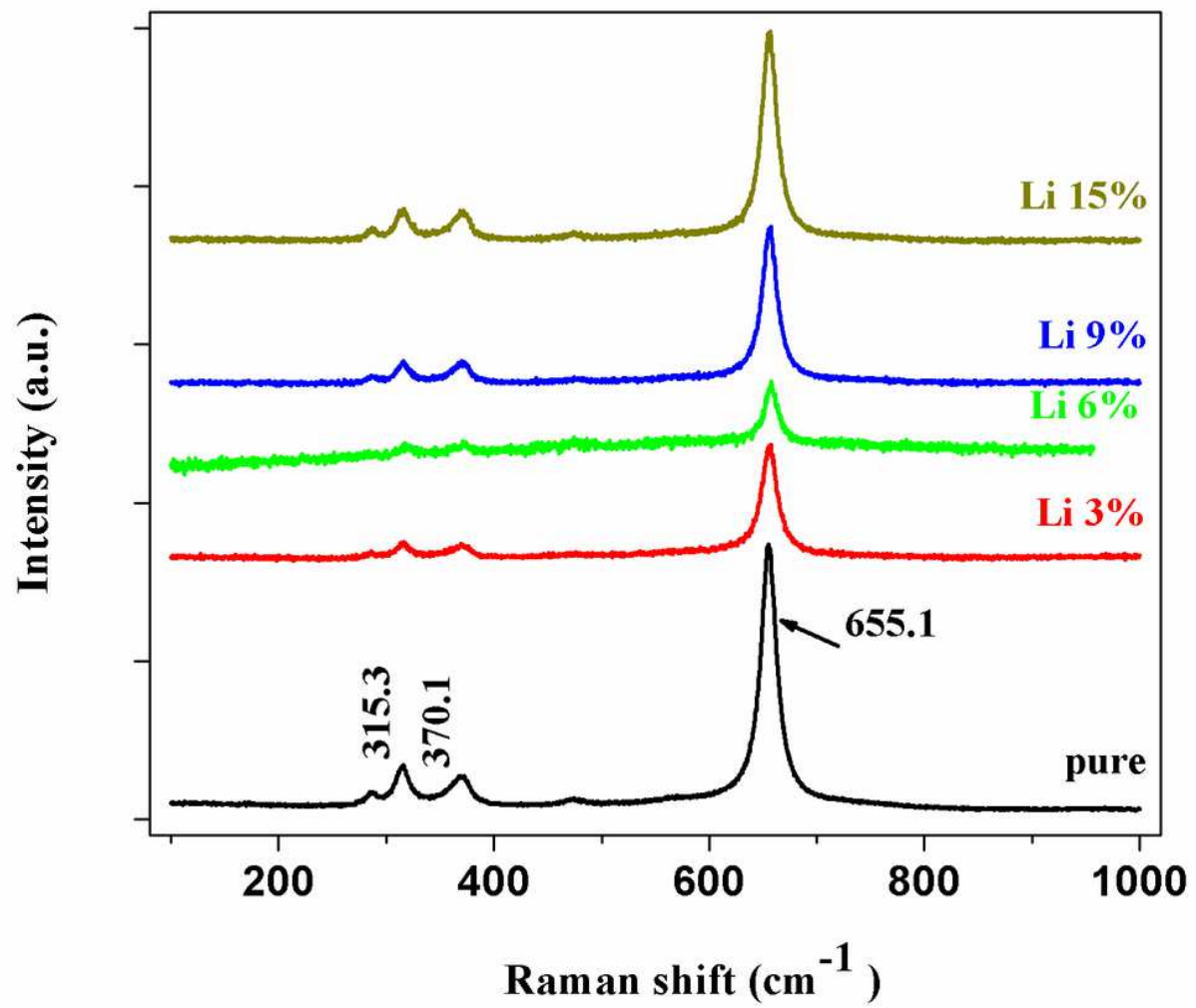


Figure 2

Raman spectra of Li/Mn₃O₄ physical mixtures thin films.

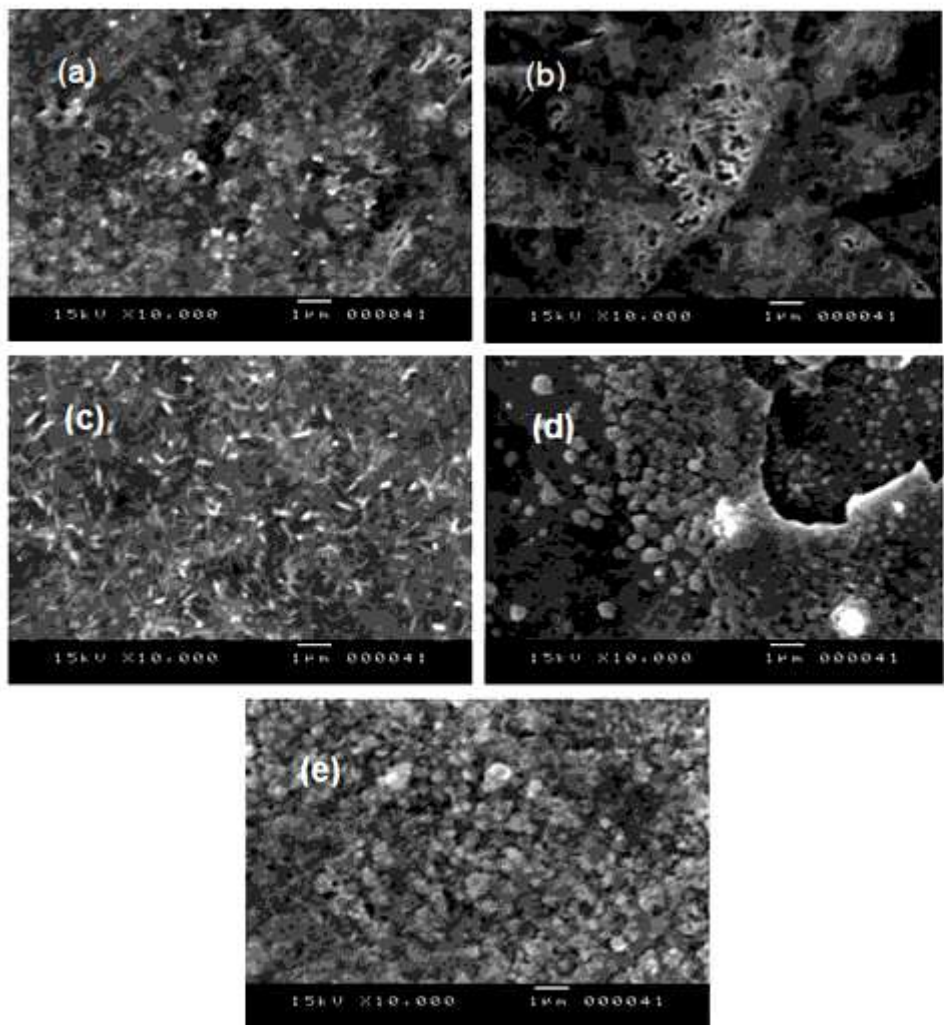


Figure 3

SEM images of Li/Mn₃O₄ thin films at different Li contents: 0% (a), 3% (b), 6% (c), 9% (d), 15% (e)

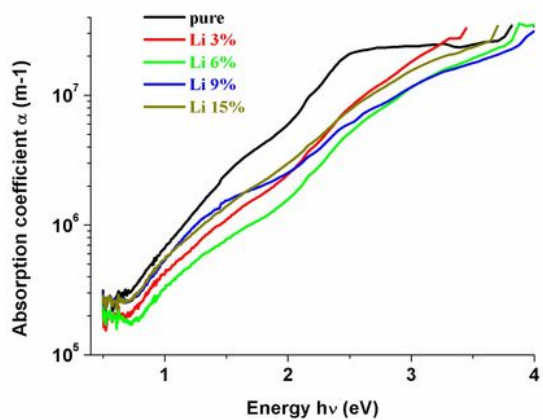
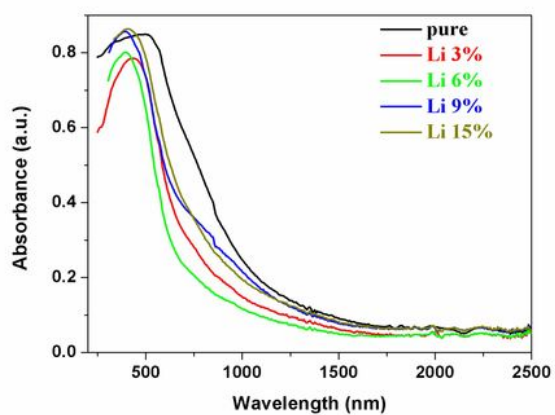
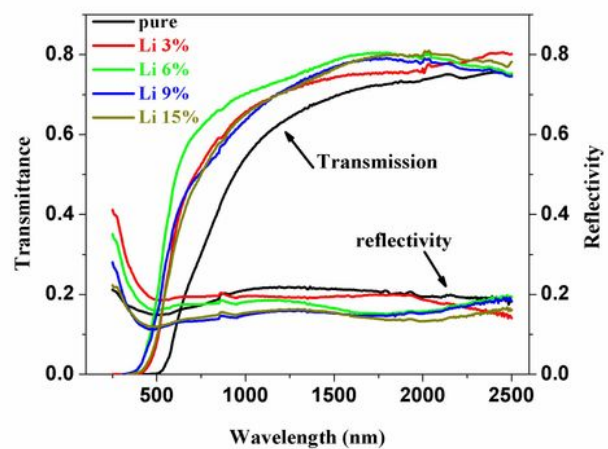


Figure 4

(a) Transmittance and reflectivity spectra of Li/Mn₃O₄ thin films. (b) Absorbance of Li/Mn₃O₄ thin films for different Li contents. (c) Absorption spectra of Li/Mn₃O₄ thin films for different Li contents.

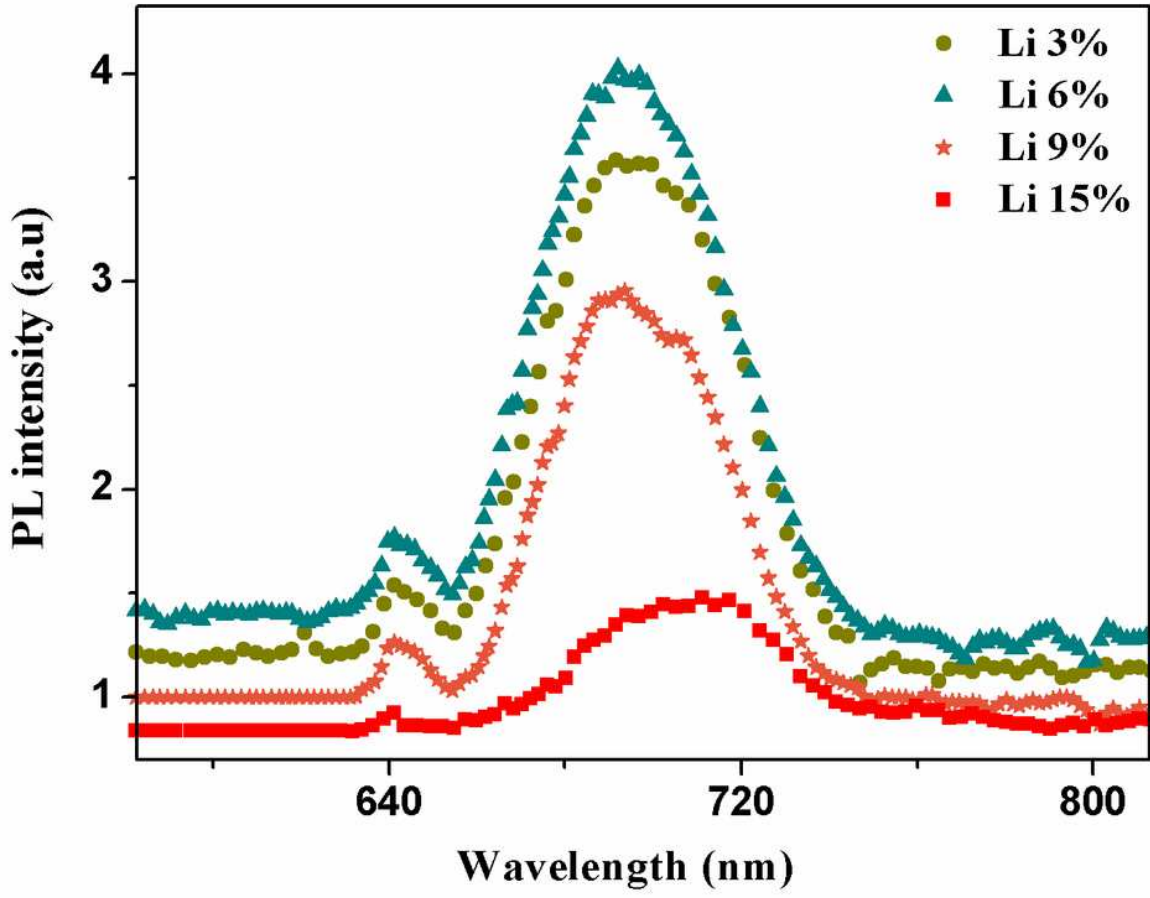


Figure 5

Photoluminescence spectra of Li/Mn₃O₄ thin films.

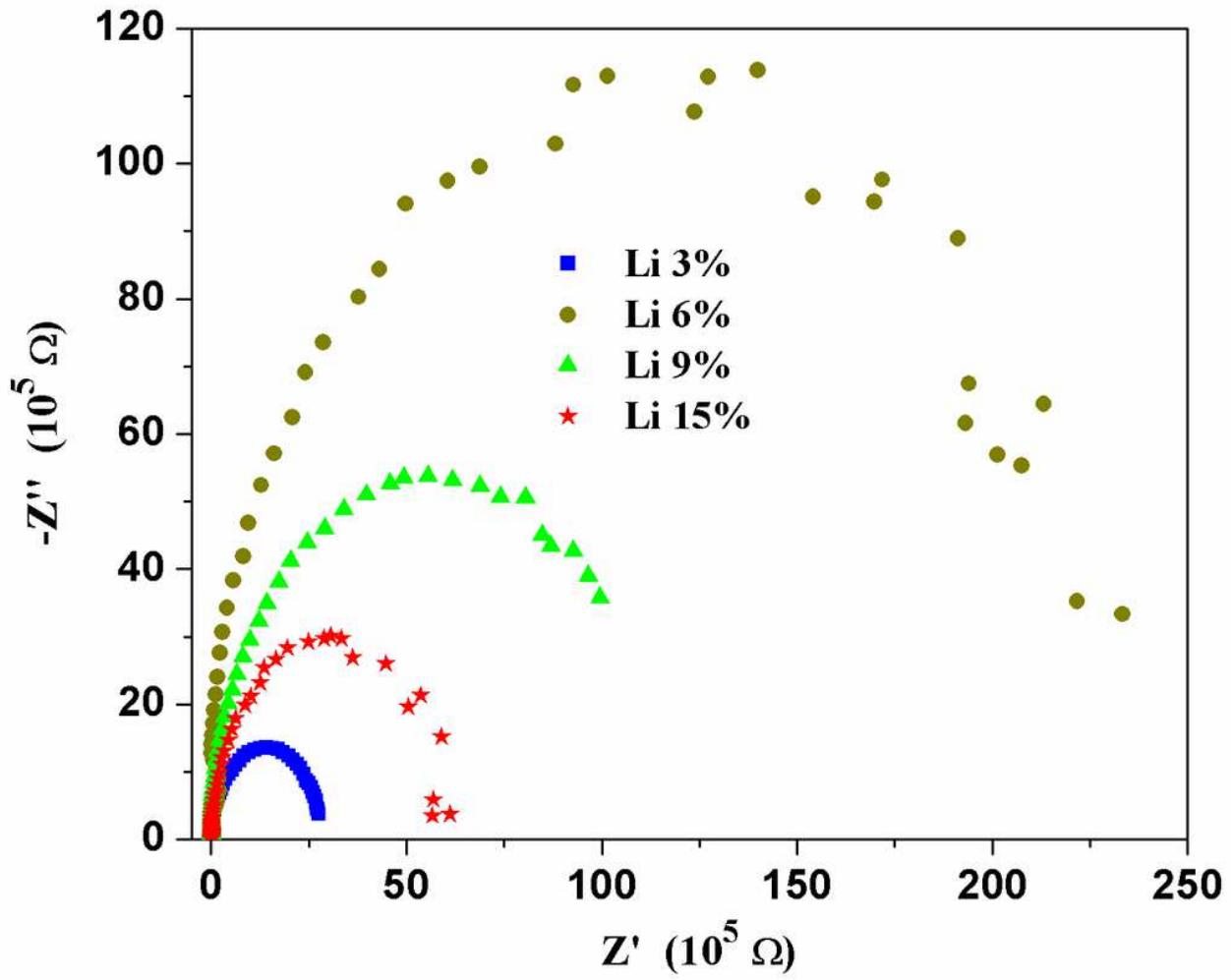


Figure 6

Complex impedance spectra of Li/Mn₃O₄ thin films.

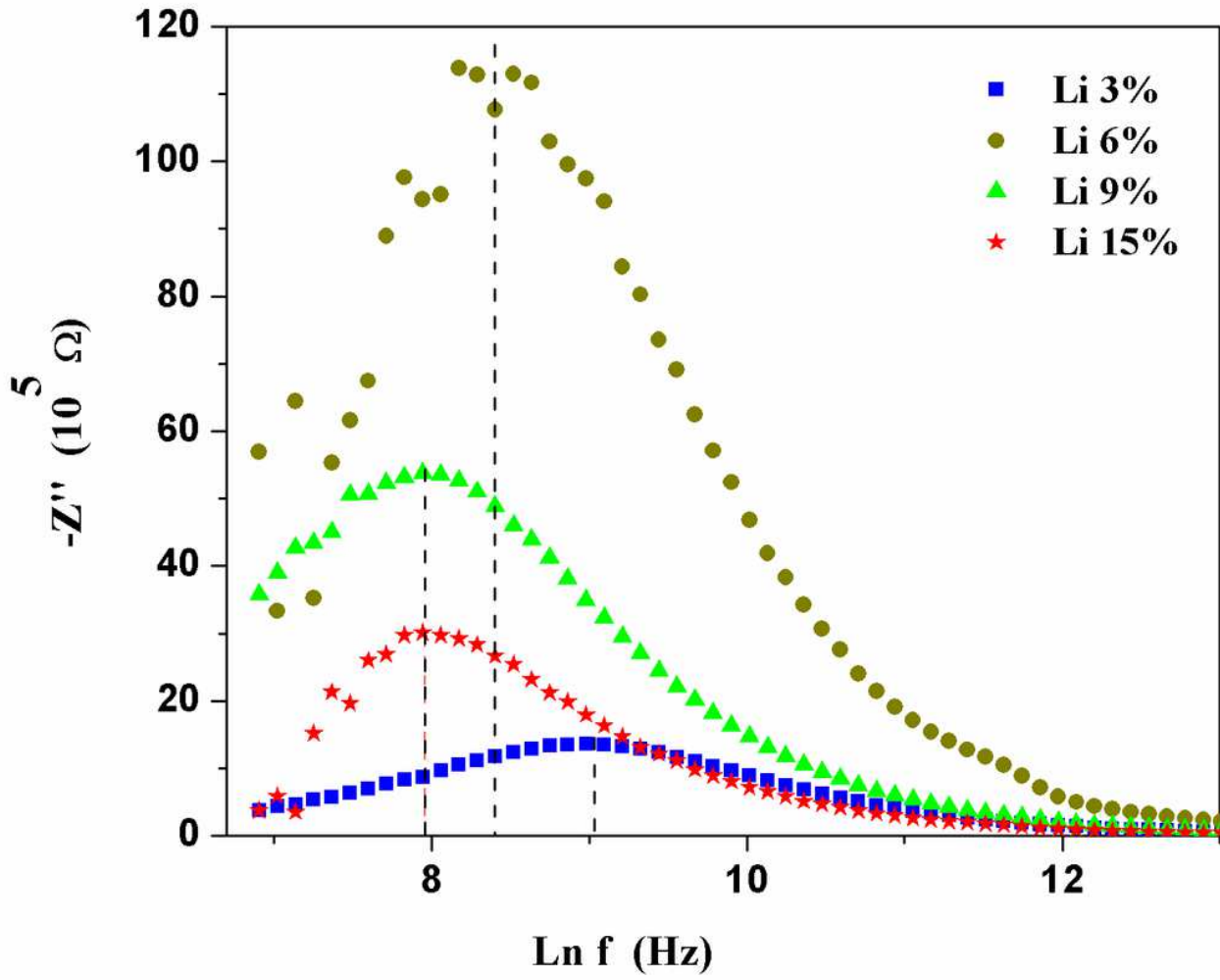


Figure 7

Impedance imaginary-part Z'' versus frequency, for Li/Mn₃O₄ thin films.

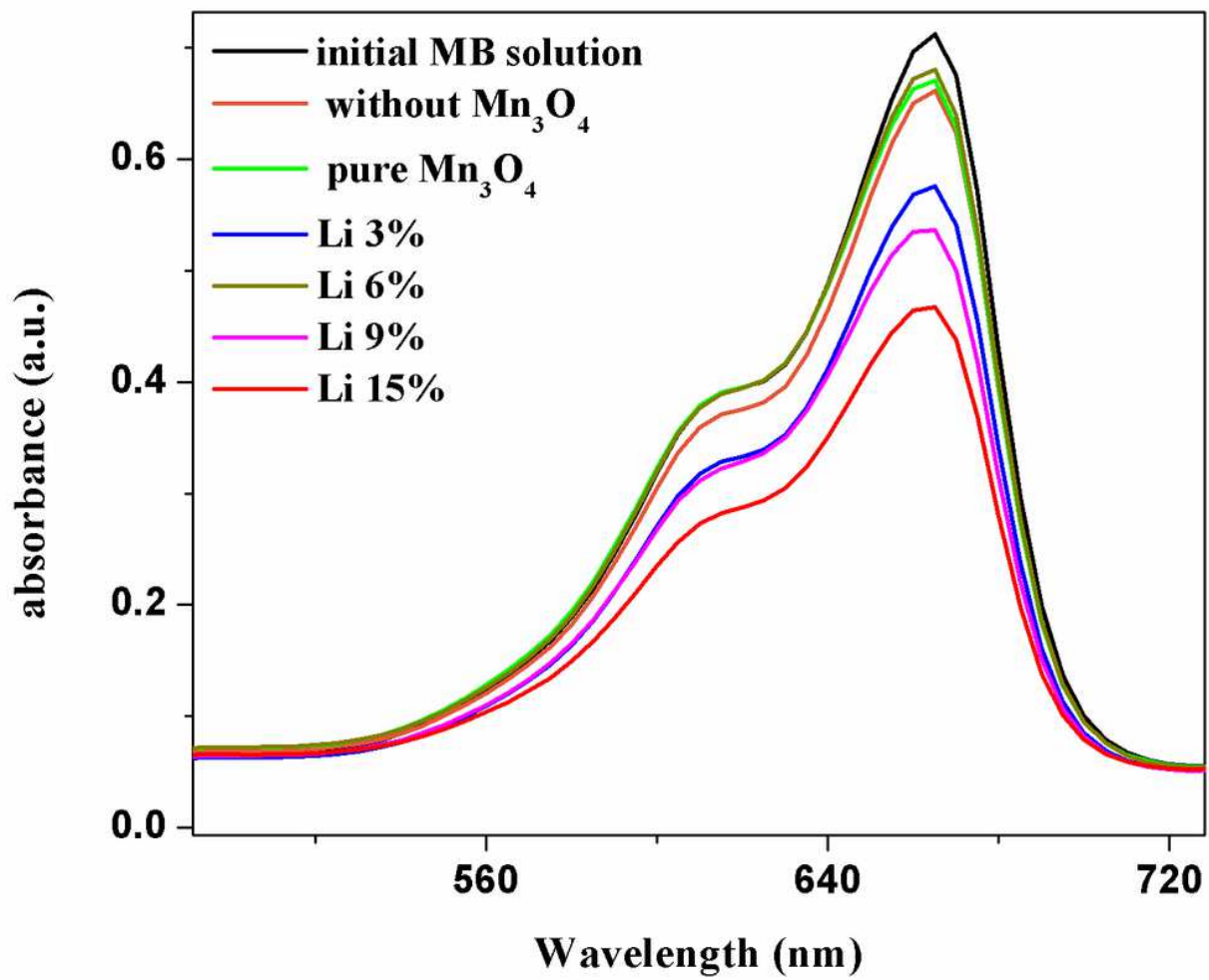


Figure 8

MB absorption spectra after degradation by Li/Mn₃O₄ thin films under UV irradiation for 2h.

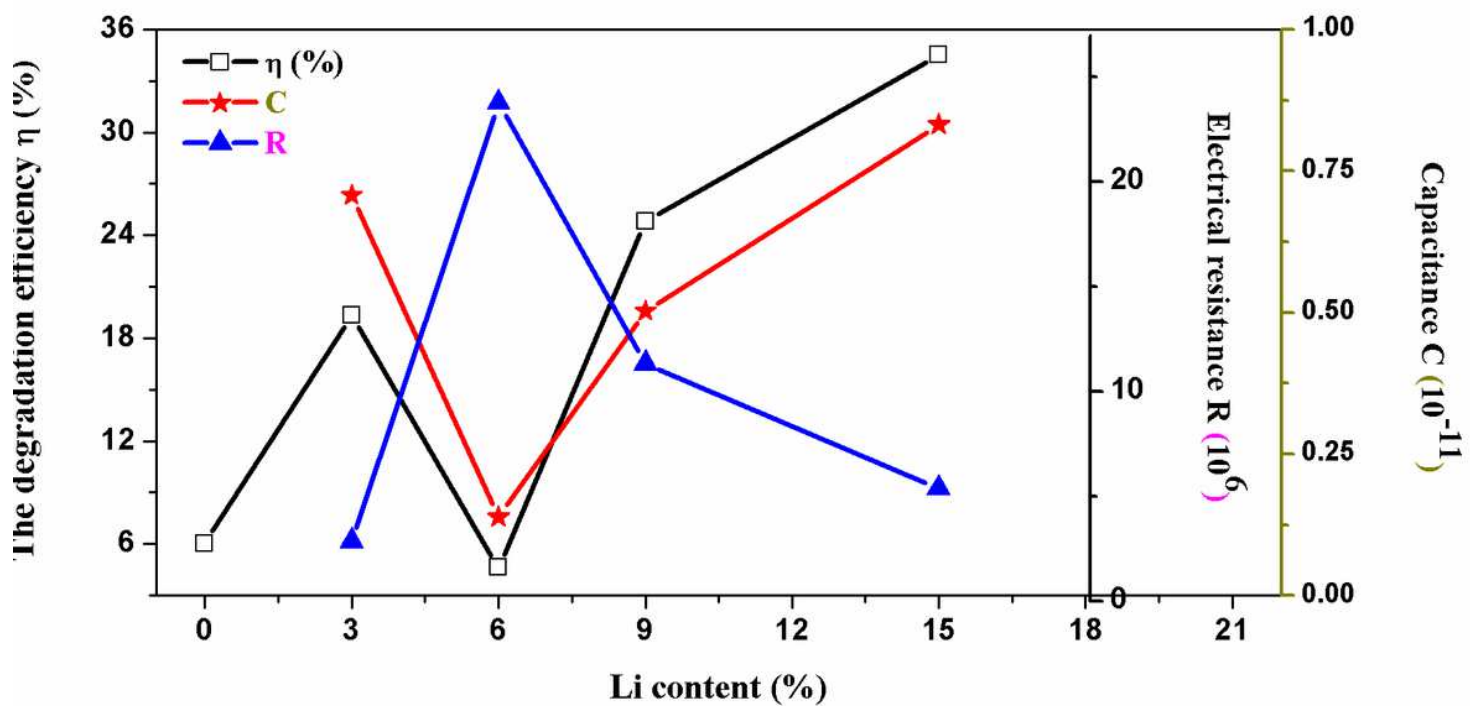


Figure 9

Degradation efficiency, electrical resistance and capacity of Li/Mn₃O₄ thin layers.

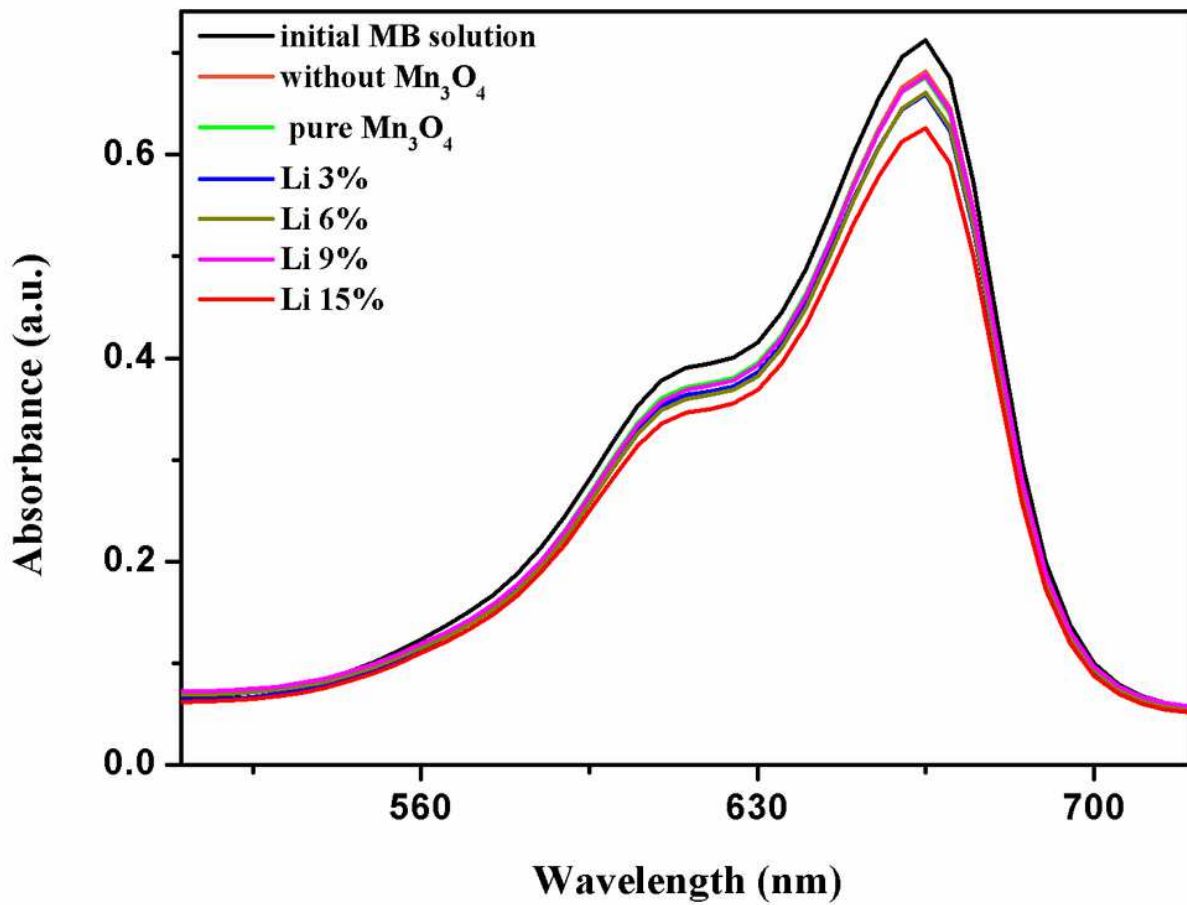


Figure 10

MB absorption spectra in presence of Li/Mn₃O₄ thin films after 2 h exposure to visible light.

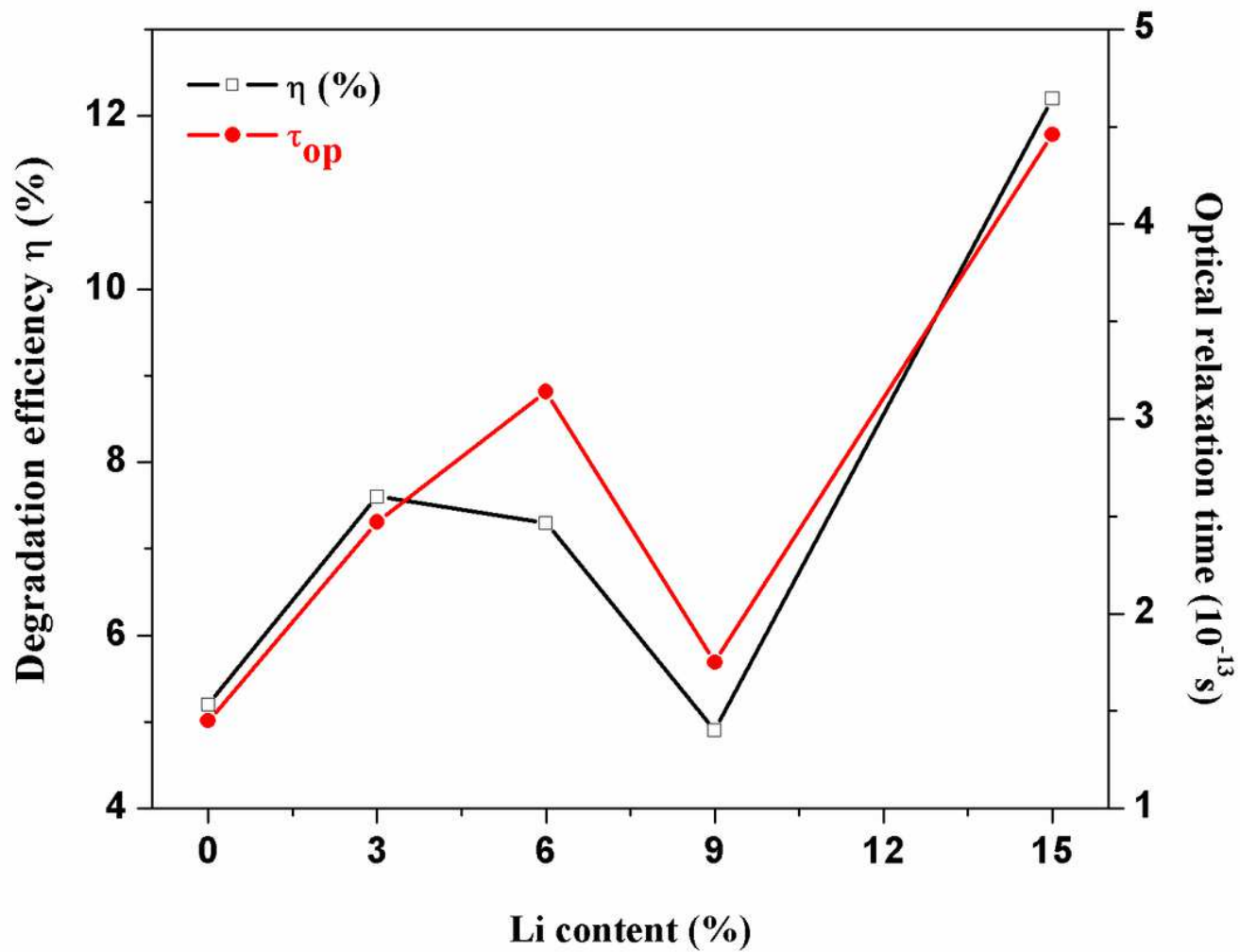


Figure 11

Variations of photocatalytic efficiency and optical relaxation time versus Li content.

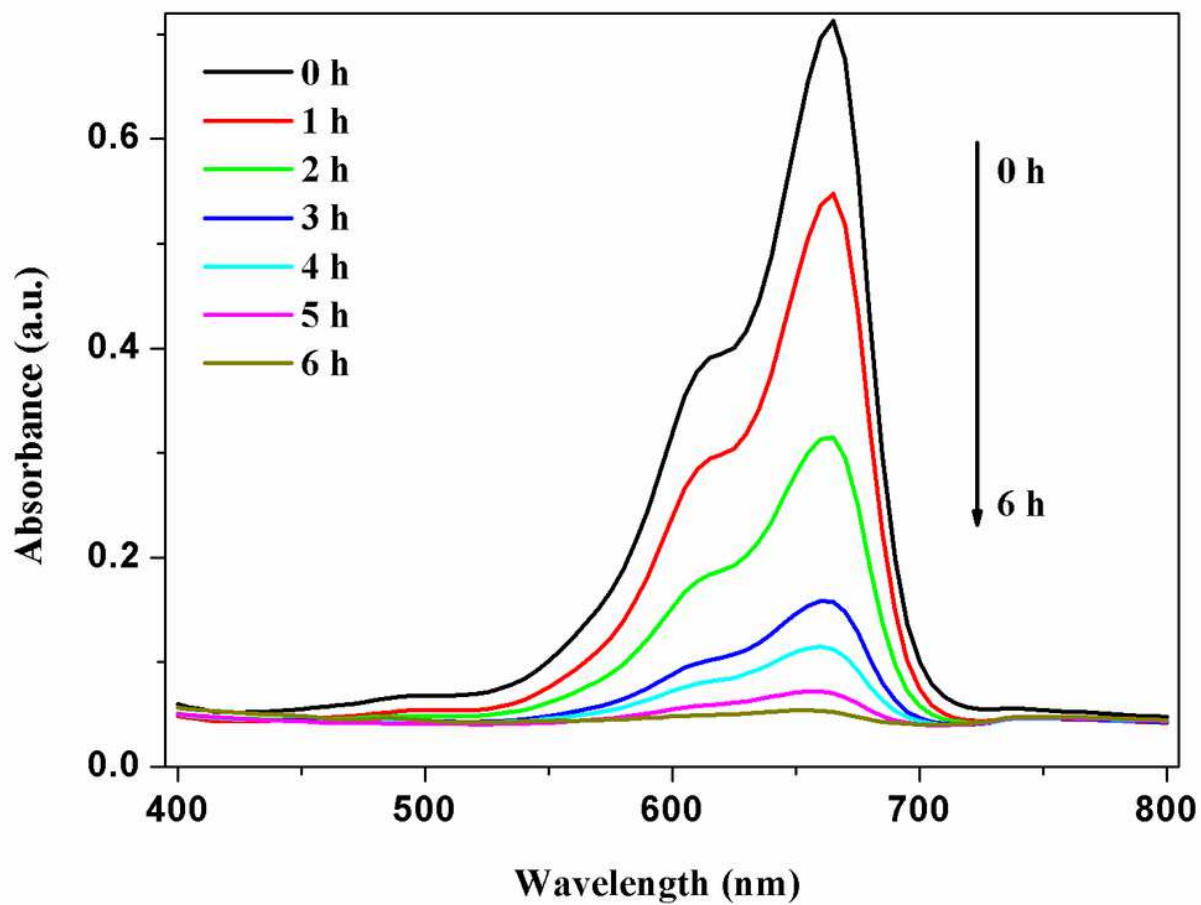


Figure 12

Absorption spectra of MB in presence of Li/Mn₃O₄ at 15% of Li as a function of sunlight exposure time.

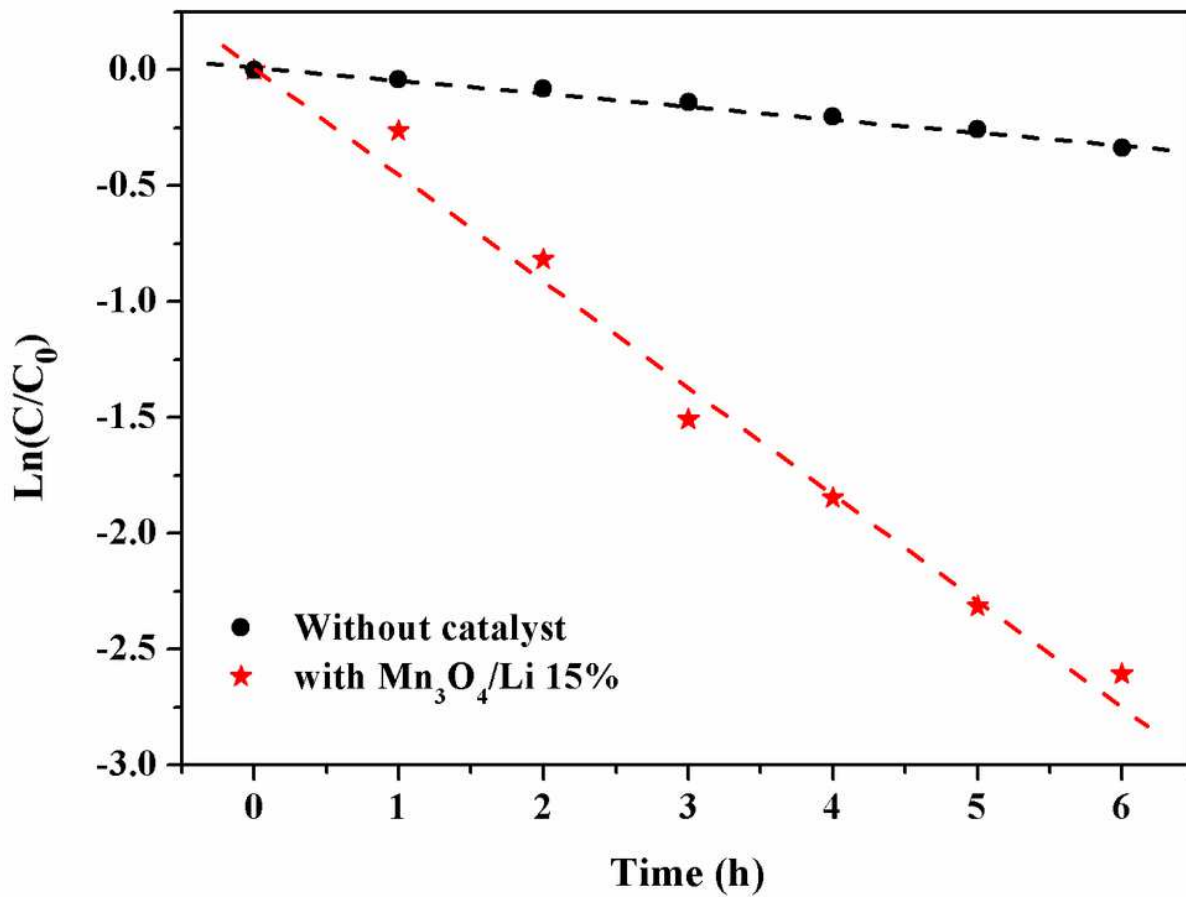


Figure 13

Photocatalytic degradation of MB by Li/Mn₃O₄ at 15% of Li, under sunlight irradiation.

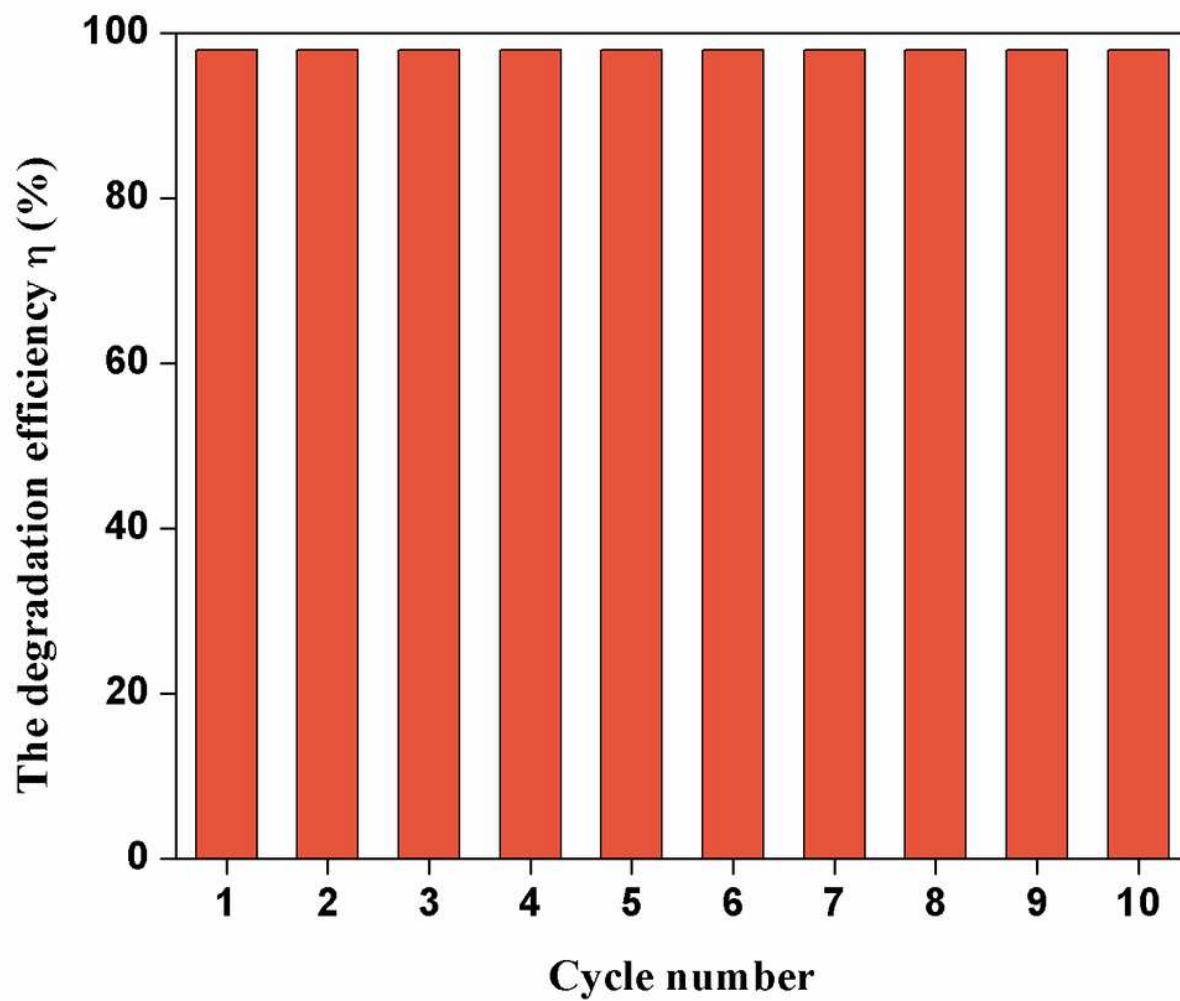


Figure 14

Stability of physical mixture Li/Mn₃O₄ at 15% of Li for photodegradation of MB under sunlight.